Angular dependence of fast-electron scattering from materials

Juri Barthel,[1,*] Mauricio Cattaneo,[1] Budhika G. Mendis,[2] Scott D. Findlay,[3] and Leslie J. Allen[4]

[1]*Ernst Ruska Centre (ER-C), Forschungszentrum Jülich GmbH, 52425 Jülich, Germany*
[2]*Department of Physics, Durham University, South Road, Durham DH1 3LE, United Kingdom*
[3]*School of Physics and Astronomy, Monash University, Clayton, Victoria 3800, Australia*
[4]*School of Physics, University of Melbourne, Parkville, Victoria 3010, Australia*

(Received 25 February 2020; revised manuscript received 8 April 2020; accepted 15 April 2020; published 12 May 2020)

Angular resolved scanning transmission electron microscopy is an important tool for investigating the properties of materials. However, several recent studies have observed appreciable discrepancies in the angular scattering distribution between experiment and theory. In this paper we discuss a general approach to low-loss inelastic scattering which, when incorporated in the simulations, resolves this problem and also closely reproduces experimental data taken over an extended angular range. We also explore the role of ionic bonding, temperature factors, amorphous layers on the surfaces of the specimen, and static displacements of atoms on the angular scattering distribution. The incorporation of low-loss inelastic scattering in simulations will improve the quantitative usefulness of techniques such as low-angle annular dark-field imaging and position-averaged convergent beam electron diffraction, especially for thicker specimens.

DOI: 10.1103/PhysRevB.101.184109

I. INTRODUCTION

Scanning transmission electron microscopy (STEM) is widely used as a tool to investigate the properties of materials [1]. High-angle annular dark-field (HAADF) STEM provides intuitive atomic-number dependent images [2] and quantitative agreement is found with simulations incorporating elastic scattering and inelastic scattering due to excitations of phonons [3], such as encapsulated in the quantum excitation of phonons (QEP) model [4]. Traditionally the HAADF signal is monitored as a function of probe position by a dedicated annular detector with an inner angle typically three to five times that of the probe convergence semiangle α and spanning tens of milliradians. The advent of fast pixelated detectors [5] now provides the ability to obtain physical insights by flexibly synthesizing images from electrons scattered through different angular ranges, so-called four-dimensional (4D) STEM [6]. For example, low-angle annular dark-field imaging is sensitive to strain in the atomic structure [7,8], while annular bright-field imaging [9], integrating signal over a range such as $\alpha/2$ to α, allows simultaneous imaging of light and heavy elements at atomic resolution.

Simulations for thicker samples, where multiple scattering is important, are an essential adjunct to quantitative interpretation of STEM images. While agreement between theory and experiment can now routinely be achieved for the range of large scattering angles typically used for HAADF STEM, this is not the case for lower scattering angles. The critical role of multiple inelastic scattering in diffraction patterns was shown by Mkhoyan *et al.* [10] who made quantitative comparisons between experimental bright-field intensities and simulations for amorphous silicon samples of about 100 nm in thickness. Including low-loss inelastic scattering in calculations that already effectively accounted for phonon excitations, they showed that an overestimate of bright-field intensities could be reduced from about 30% down to a few percent. The low-loss inelastic scattering usually neglected in calculations comprises electron-electron interactions causing an energy loss of the probing electron typically below 50 eV, such as plasmon excitations and interband transitions. Mkhoyan *et al.* concluded that "theoretical diffraction patterns and, therefore, high-resolution images also must contain inelastic scattering for an absolute intensity comparison with experiment" [10].

More recent examples of the lack of agreement between the measured angular dependence of scattering and theory using standard simulations incorporating only elastic scattering and phonon excitations were provided by Müller-Caspary *et al.* [11] who used what they dubbed angle-resolved STEM to explore several semiconductor specimens. Effectively using a series of detectors, each incrementally covering a small angular range, they found an underestimate of measured intensities compared to simulations at angles roughly three to four times α (9 mrad). Their experimental results for the case of pure Si $\langle 110 \rangle$ with 162 nm sample thickness are reproduced in Fig. 1, where the dashed red line shows the result of a simulation in the QEP model [4]. The simulation clearly diverges from the experimental data around 35 mrad, as do other simulations shown in Ref. [11]. Here, the experimental data were normalized to the right-most data point. Müller-Caspary *et al.* surmised that the discrepancy might be related to low-loss inelastic electron scattering, especially for samples $\gtrsim$10 nm thick.

We will show that taking into account low-loss inelastic scattering reproduces the experimental data in Fig. 1 and demonstrate that this provides an improved level of agreement

*Corresponding author: ju.barthel@fz-juelich.de

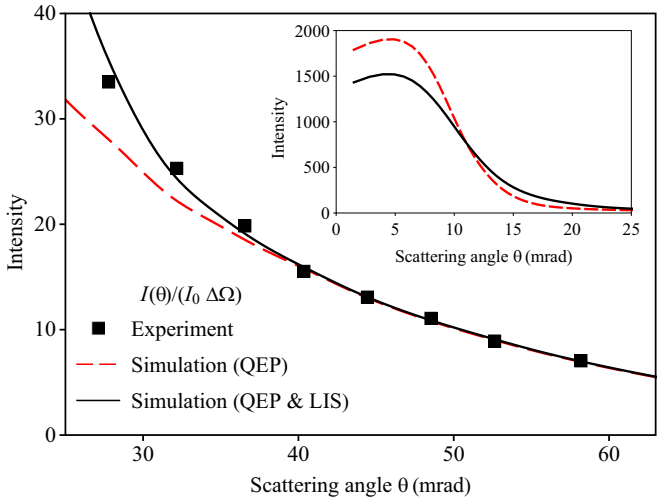

FIG. 1. Angular dependence of scattering $I(\theta)$ plotted as a function of scattering angle in fractions of the incident beam current I_0 and normalized to the solid angle $\Delta\Omega$ of the annular integration regions, for 300-keV electrons on ⟨110⟩ Si. A probe convergence of 9 mrad was used and the results represent an average over probe position. Simulations in the QEP model are shown by the red, dashed curve and simulations including additional low-loss inelastic scattering (LIS) by the solid, black curve. The experimental data were taken from Ref. [11]. The inset shows simulated results for the angular range below 25 mrad.

between experiment and simulation for the full angular range of scattering from 0 to 64 mrad by means of a new data set. The data were acquired with a modern pixelated detector under conditions relevant for 4D-STEM imaging and with better than 1 Å spatial resolution. To simulate the low-loss inelastic scattering, we extended the Monte Carlo based approach introduced recently to include plasmon scattering in multislice simulations [12] to a more general framework by applying it to encompass all the low-loss inelastic scattering (with the exception of phonon excitations) into the small angles that usually dominate an electron-energy-loss spectrum. The model of Mkhoyan *et al.* [10] is also general in that sense, but the present approach has the further advantages that subsequent channeling of the inelastic part of the beam is included naturally within a QEP or frozen phonon framework and that the statistical distribution of multiple inelastic-scattering events is more robustly handled (cf. using only the mean number of events).

We will also explore several other effects which may explain or contribute to the difference between the QEP model and experiment. We will consider the effects of alternative atomic form factors and, in particular, the modifications due to ionic bonding. We also explore varying the temperature (Debye-Waller) factors, the contribution of amorphous layers on the surfaces of the specimen, and the role of static displacements of atoms in the sample.

II. GENERALIZED MODEL FOR LOW-LOSS INELASTIC SCATTERING

We will use a generalization of the Monte Carlo approach in Ref. [12] that entails broadening some aspects of the standard plasmon excitation model to describe low-loss inelastic scattering. The relationship of the critical angle to the energy loss [13] is relaxed. Also, the mean free path for inelastic scattering is no longer necessarily that suggested by a plasmon model and could, in the absence of an experimental value, be a free parameter in simulations and also vary as a function of depth in the specimen. It is worth noting that mean free paths measured by a spectrometer with an entrance aperture limiting collection angles may not be applicable for simulations where electrons that inelastically scatter through all angles contribute, implying a smaller value for the mean free path. However, the relationship between the characteristic angle for inelastic electron-electron scattering θ_E to the average energy loss ΔE and to the primary electron energy E_0, namely $\theta_E = \Delta E/(2E_0)$, is maintained.

We work in the context of the quantum excitation of phonons model [4] which is extended by deciding at each slice in the multislice calculation how many low-loss inelastic-scattering events occur at that slice using a generator $P(\mu)$ of integer Poissonian random numbers. The mean value $\mu = \Delta z/\lambda$ of the random distribution is determined by the thickness Δz of the slice and the mean free path λ for inelastic scattering (or, put another way, the inverse of the strength of the inelastic scattering) in that slice. This approach is consistent with the calculation of the probability for single bulk plasmon generation in Eq. (2) of Ref. [10] and with a random scattering depth as calculated by Eq. (2) of Ref. [12].

A constant value of the parameter λ is appropriate for describing the effect of bulk plasmon excitations in a material, where the probability of inelastic scattering is distributed equally over the sample volume. For other phenomena, such as surface plasmons, where a uniform distribution of scattering probability would not apply, the model can be generalized by allowing λ to become a function of depth. However, to maintain simplicity here, we will apply the model using a constant effective λ to describe experimental data. In this approximation it can be expected that λ will change between measurements taken at different sample thickness if surface effects play a significant role in the inelastic scattering.

If an inelastic event is triggered in a particular slice, i.e., $P(\mu) > 0$, then it is assumed that the consequence is scattering through an angle

$$\theta = \theta_E \sqrt{\left(\frac{\theta_c^2 + \theta_E^2}{\theta_E^2}\right)^{R_1} - 1}, \tag{1}$$

which is a corrected version of Eq. (4) in Ref. [12] (which was misprinted, although the correct expression was used in the simulations) and through an azimuthal angle

$$\phi = 2\pi R_2. \tag{2}$$

In Eq. (1), θ_E is the characteristic angle [14], θ_c is the so-called critical angle, and R_1 is a random number from a uniform probability distribution in the interval [0,1], as is R_2 in Eq. (2). The angle θ_E is characteristic of the Lorentzian distribution of the inelastic scattering and θ_c imposes an angular limit on this scattering. In the usual plasmon model θ_c is determined by the point at which single-electron excitations become permissible [13] and other modes such as exciton creation and ultraviolet-light emission also exist [15]. However, there is

evidence of collective-mode oscillation for scattering through angles greater than θ_c [16]. In addition to the phonon excitations already incorporated in the QEP model, here we want to also effectively model all low-loss inelastic scattering, including plasmons for conducting materials as well as interband transitions for insulators. Therefore, larger values of θ_c are appropriate.

Multiple inelastic scattering is also inherent in the repeated decisions on the occurrence of inelastic events made over a multislice pass. For a sufficiently thick sample multiple scattering can be seen in the energy-loss spectrum, e.g., as shown in Fig. 2(a) of Ref. [12]. A sufficient number of passes must be accumulated to reach convergence with respect to both the phonon excitations and the low-loss inelastic scattering.

The Monte Carlo procedure to simulate low-loss inelastic scattering has been implemented by extending existing multislice code in the Dr. Probe [17] and μSTEM software [18], providing cross checks on the simulations. We tilt the probe wave function with respect to the specimen for each inelastic event occurring at a given slice through angles generated by Eqs. (1) and (2). This is done by effectively applying a phase ramp $\exp(2\pi i \Delta\mathbf{k}_t \cdot \mathbf{r})$ in real space where

$$\Delta\mathbf{k}_t = k_0 \begin{pmatrix} \theta\ \cos\phi \\ \theta\ \sin\phi \end{pmatrix} \tag{3}$$

is the change in transverse wave vector due to low-loss inelastic scattering, with k_0 denoting the wave number of the incident probe electrons in vacuum, and $\mathbf{r}$ being a position vector in the xy plane normal to the optic axis. This can be implemented numerically in an efficient way by shifting the wave function in its Fourier space representation. Binning to shifts equal to those represented by discrete sampling of wave functions maintains the periodic boundary conditions usually applied in multislice calculations. Thus the effect of low-loss inelastic scattering is modeled as scattering through a small angle or succession of small angles, since electron-electron energy losses of at most tens of eV suggest a θ_c well within the typical bandwidth limits used in QEP simulations (a few hundreds of milliradians). The major effect is a redistribution of intensity in the diffraction plane over an angular range limited by θ_c, or a few multiples of θ_c when multiple excitations are pertinent. For the case of a STEM probe, the redistribution of intensity will essentially be from the bright-field disk into the adjacent dark-field region. This should lead to lower bright-field intensities and higher intensities in the low-angle dark-field region when compared to simulations neglecting low-loss inelastic scattering.

III. APPLICATION TO EXPERIMENTAL DATA

Returning to the QEP and LIS simulation in Fig. 1 (the solid, black curve), this was performed assuming the following parameters: $\lambda = 100$ nm, $\theta_E = 0.034$ mrad, and $\theta_c = 15.0$ mrad. The critical angle required to describe the angular dependence of scattering for electrons with 300-keV kinetic energy corresponds to a larger limit of momentum transfer when compared to theoretical and experimental values given in the literature [14,19,20]. Results for the angular range 25–60 mrad are shown in Fig. 1, with those for smaller angles shown in the inset. The inclusion of the additional low-loss inelastic scattering largely resolves the discrepancy between experiment and theory. The inset shows the expected "flip over" in intensity inside 25 mrad needed for flux conservation.

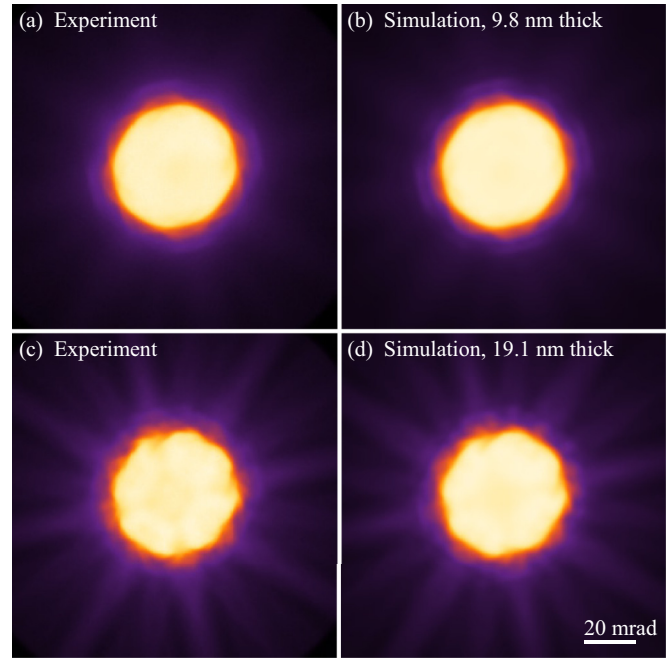

FIG. 2. Position averaged convergent beam electron diffraction (PACBED) matching for a high-resolution 300-keV electron probe incident on ⟨001⟩ $SrTiO_3$ for (a) experiment and (b) simulation for a specimen of thickness 9.8 nm and (c) experiment and (d) simulation for a specimen of 19.1 nm. In each case both the experimental and simulated diffraction patterns are shown on the same scale with lower intensities amplified to enhance the contrast at larger scattering angles. The scale bar shown in (d) applies to all subfigures.

A more precise angular range can be measured using a pixelated detector in the diffraction plane of the microscope. In particular, such measurements include bright field and lower scattering angles not accessed by Müller-Caspary *et al.* [11] together with larger angles not evaluated by Mkhoyan *et al.* [10]. Position averaged convergent beam electron diffraction (PACBED) patterns of $SrTiO_3$ in ⟨001⟩ orientation, as shown in Figs. 2(a) and 2(c), were acquired using a probe C_S-corrected microscope at 300 kV accelerating voltage [21]. The instrument is equipped with a Merlin Medipix 3 detector for recording diffraction patterns on a 256×256 array of pixels [22]. Diffraction projection, detector gain correction factors, and the frequency modulation transfer function have been carefully calibrated to enable accurate modeling of diffraction patterns by multislice simulations.

A thin lamella of $SrTiO_3$ in ⟨001⟩ orientation was extracted from a commercial substrate material (Crystec GmbH, Berlin, Germany) by focused ion-beam milling with an FEI Helios NanoLab 460F1 FIB-SEM [23]. The sample was further thinned by 900-eV Ar ion milling and finally polished using a 500-eV Ar ion beam in a Fischione Model 1040 NanoMill (E.A. Fischione Instruments, Inc., Export, PA, USA).

Two areas on the lamella, which were of different thicknesses, were the subject of 4D-STEM experiments and PACBED patterns were synthesized from the data by averaging over scan areas containing a discrete number of projected ⟨001⟩ $SrTiO_3$ unit cells. For each of these measurements, the recorded intensity is put on the same scale as the simulations by normalization as a fraction of the incident beam current. The incident beam current was experimentally determined by recording a second data set under identical conditions without the sample present shortly after each measurement. After correction of the measured linear projection distortion, an average probe convergence semiangle of 23.5 mrad was measured and a residual twofold asymmetry of 3.4% at an orientation of 46° to the horizontal detector axis could be observed in the image of the probe forming aperture without the sample. The asymmetry of the effective probe forming aperture was included in the simulations in order to achieve a better agreement of experimental and simulated diffraction patterns.

The PACBED pattern shown in Fig. 2(a) was deduced to be from an area of thickness 9.8 nm (25 unit cells) by matching simulated intensities to the experiment in the range of scattering angles from 50 to 60 mrad. This thickness is the same as that one obtains when maximizing the correlation between simulation and experiment for the two-dimensional PACBED pattern. Using the standard PACBED pattern matching approach (minimizing an ℓ^2-norm metric) one obtains a thickness of 10.2 nm (26 rather than 25 unit cells) but for large probe forming apertures as used here this approach has been shown to be less robust [24].

The simulation corresponding to Fig. 2(a) is shown in Fig. 2(b) on the same scale as the experimental pattern and accounts for a sample tilt of (0.1, −0.8) mrad relative to the ⟨001⟩ zone axis. The pair of angles refers to the components of tilt along the ⟨100⟩ and the ⟨010⟩ directions of the crystal lattice. A total of 12 000 multislice passes were accumulated for the PACBED simulations to ensure convergence of the Monte Carlo approach. The PACBEDs were generated by averaging diffraction patterns while scanning the probe across a projected unit cell of the structure. Phonon excitations were simulated using random variates of uncorrelated atomic displacements and low-loss inelastic-scattering events were generated as described in Sec. II.

The second experimental PACBED pattern, shown in Fig. 2(c), is matched in the region 50–60 mrad by a simulation using a thickness of 19.1 nm (49 unit cells) at sample tilt (−2.6, −1.0) mrad as in Fig. 2(d). This thickness is at variance with the thickness deduced from pattern correlation or ℓ^2-norm matching, which yield 23.0 nm (59 unit cells) and 23.4 nm (60 unit cells) respectively.

The angular dependence of the PACBED intensities of Figs. 2(a) and 2(b) are shown quantitatively in Fig. 3(a). The plot compares the experimental data with a simulation in the QEP model (red, dashed curve), which shows clear discrepancies from experiment in the angular range 25–45 mrad. The solid, black curve shows a simulation that, in addition, includes low-loss inelastic scattering (LIS) in the generalized model using the following parameters: $\lambda = 60$ nm, $\theta_E = 0.05$ mrad, and $\theta_c = 25$ mrad. The values quoted provided the best match to the data. The choice of characteristic angle is motivated by low-energy-loss spectra recorded for $SrTiO_3$ which extend over a range from 3 to 60 eV and are dominated by interband transitions [25,26]. Looking at the spectrum globally or, alternatively, imagining it as a lower resolution energy-loss curve, we have inelastic scattering with an average energy loss at 30 eV, from which we infer our characteristic scattering angle $\theta_E = 0.05$ mrad. Mean free path and critical angle were then adjusted in simulations to achieve the best agreement with the experiment, as made explicit in Fig. 3(b).

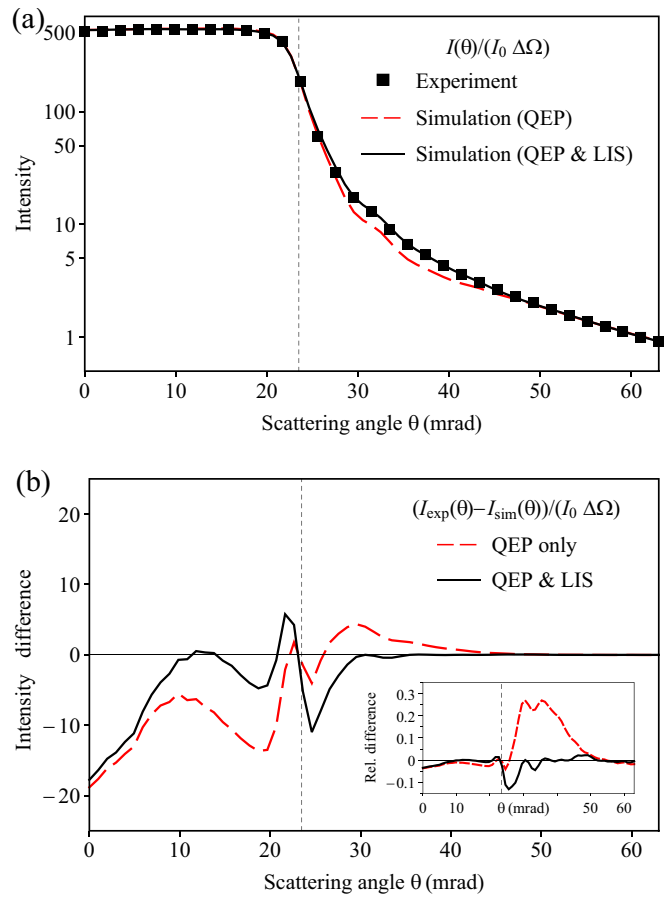

FIG. 3. PACBED intensity $I(\theta)$ as a function of scattering angle in fractions of the incident beam current I_0 and normalized to the solid angle $\Delta\Omega$ of the annular integration regions. Vertical dashed lines mark the probe convergence semiangle of 23.5 mrad. (a) Experimental results of Fig. 2(a) in comparison to QEP simulations (dashed, red line) and extended simulations in the QEP model including LIS (solid, black line), plotted on a logarithmic scale. (b) Intensity difference between experiment and simulations plotted on a linear scale. Inset is the same data relative to the measured intensities, emphasizing a significant improvement in the low-angle dark-field region.

Results similar to those in Fig. 3 are shown for the thicker specimen (19.1 nm) in Fig. 4. However, in the generalized model for low-loss inelastic scattering the effective mean free path to describe the experimental data is 140 nm in this case. The increase of the mean free path with increasing sample thickness is a consequence of applying a simplified model with constant λ to thin samples where surface plasmon excitations are known to have a significant

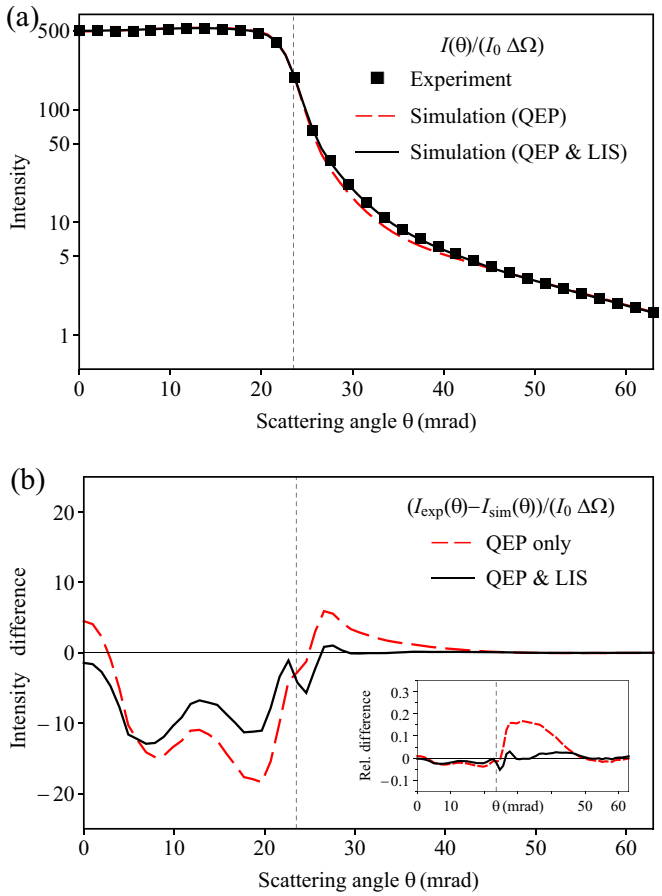

FIG. 4. PACBED intensity $I(\theta)$ as a function of scattering angle in fractions of the incident beam current I_0 and normalized to the solid angle $\Delta\Omega$ of the annular integration regions. Vertical dashed lines mark the probe convergence semiangle of 23.5 mrad. (a) Experimental results of Fig. 2(c) in comparison to QEP simulations (dashed, red line) and extended simulations in the QEP model including LIS (solid, black line), plotted on a logarithmic scale. (b) Intensity difference between experiment and simulations plotted on a linear scale. Inset is the same data relative to the measured intensities, emphasizing a significant improvement in the low-angle dark-field region.

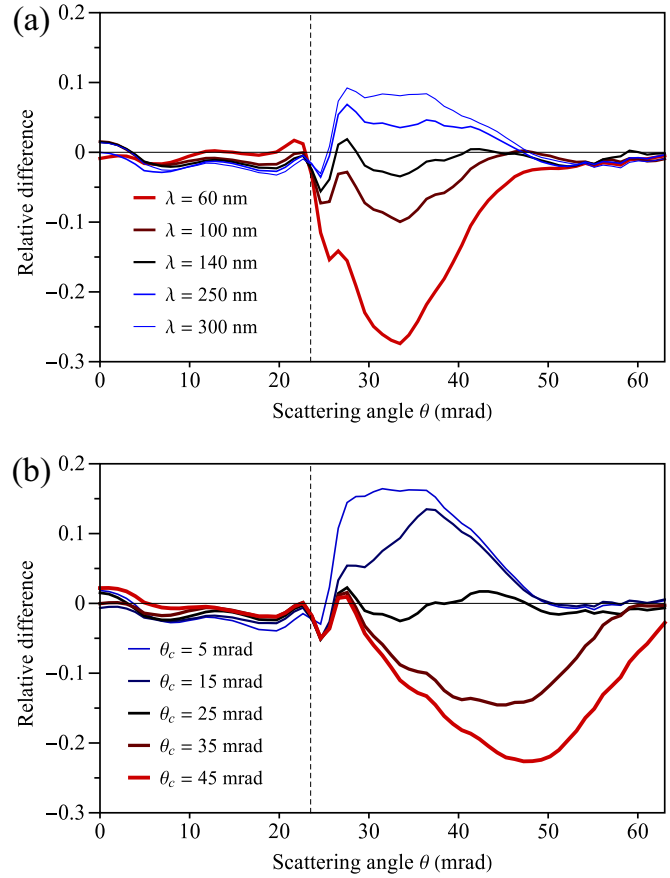

FIG. 5. Relative difference between experiment and simulations, $[I_{exp}(\theta) - I_{sim}(\theta)]/I_{exp}(\theta)$, for simulations using different values of λ and θ_c with the other parameters as in the experimental case of Figs. 2(c) and 4.

effect [3]. Distributing the probability of plasmon scattering at the two sample surfaces uniformly over an increasing sample volume reduces the probability of inelastic scattering per unit volume, which is accounted for by an effective larger mean free path for the thicker sample in the approximate model.

The influence of the mean free path λ and of the critical angle θ_c on the dependency of scattering as a function of scattering angle is shown in Figs. 5(a) and 5(b) respectively. The plot for λ is straightforward to interpret: the amount of inelastic scattering increases with decreasing mean free path. Increasing θ_c allows inelastic scattering towards larger angles according to Eq. (1). What can be seen in Fig. 5(b) for a small critical angle ($\theta_c = 5$ mrad) is that the relative difference between experiment and simulation is large and positive in the dark-field region and comparable to the relative difference plot of a pure QEP simulation, as shown by the red dashed curve in the inset of Fig. 4(b). With increasing θ_c, an increasing fraction of the inelastic scattering is towards larger angles, leading to a decrease of the relative difference. This effect starts to become visible in the curve for $\theta_c =$ 15 mrad in the angular range just above the semiconvergence angle. For critical angles larger than that used for the best match ($\theta_c = 25$ mrad), a too large fraction of the inelastic scattering is towards larger angles and the relative difference becomes increasingly negative. Although the two plots in Fig. 5 show general similarities upon variations of mean free path and critical angle, a convincing fit between experiment and simulation could only be found for one pair of the two parameters.

Despite the almost perfect modeling of the intensity as a function of scattering angle by the redistribution of intensity due to low-loss inelastic scattering, we still find a residual overestimation of the total electron flux in calculations which is mainly located in the bright-field region, as is visible in Figs. 3(b) and 4(b). Relative to the flux of the unscattered beam, 95.8% of the probe electrons are measured within scattering angles from 0 to 64 mrad in the case of 19.1-nm-thick $SrTiO_3$ in experiments, whereas the best fitting QEP and LIS calculation predicts 97.3%.

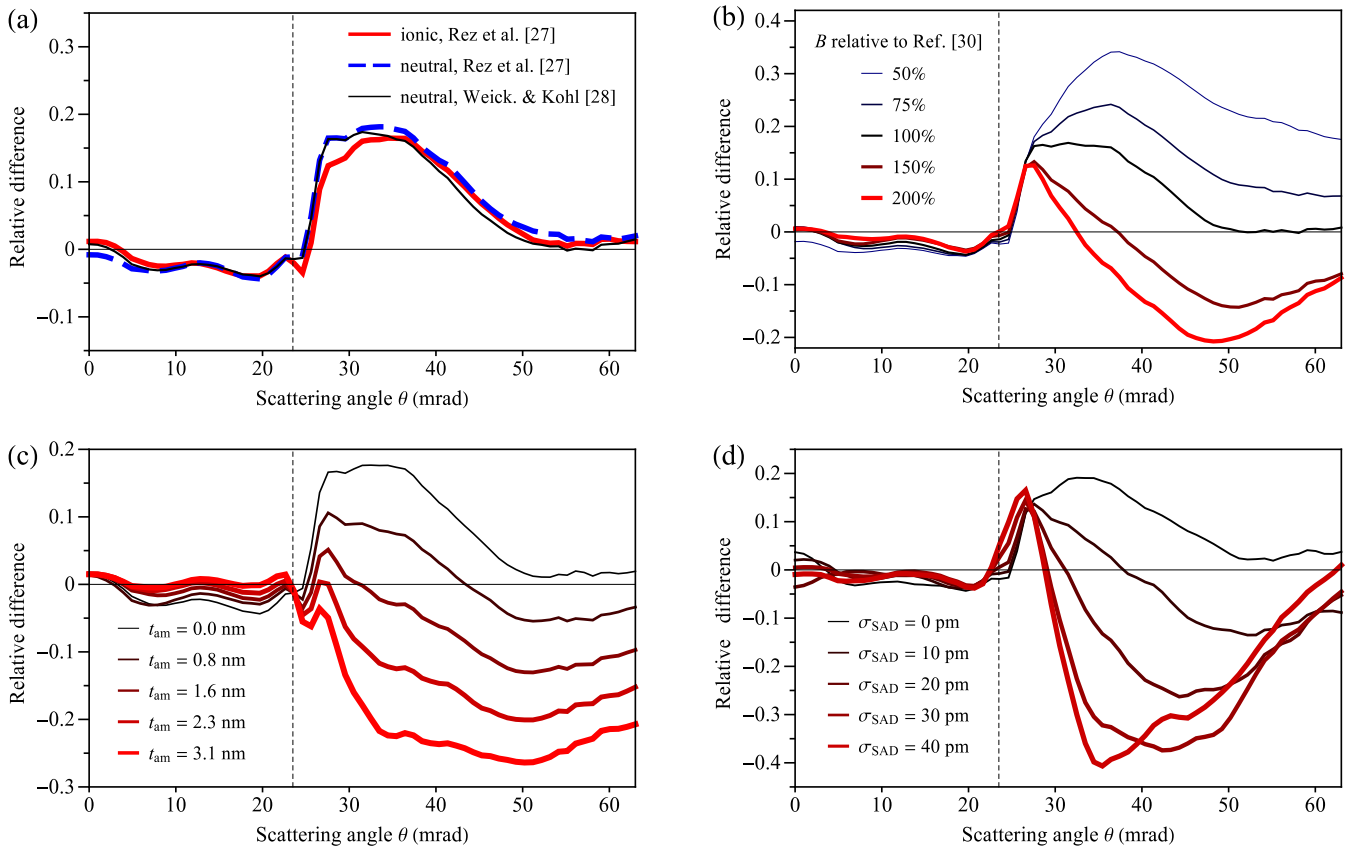

FIG. 6. Relative difference between experiment and simulations, $[I_{exp}(\theta) - I_{sim}(\theta)]/I_{exp}(\theta)$, for simulations taking into account (a) ionic bonding, (b) variation of isotropic temperature factors B, (c) amorphous layers, and (d) static displacements with the other parameters as in the experimental case of Figs. 2(c) and 4.

IV. OTHER POSSIBLE FACTORS AFFECTING THE ANGULAR DISTRIBUTION

A question which should be asked is whether there are other effects which may explain or contribute to the difference between the QEP model and experiment. We will consider the effects of alternative atomic form factors and, in particular, ionic bonding, varying the Debye-Waller factors, amorphous layers on the surfaces of the specimen, and, lastly, static displacements of atoms. All simulations in this section were for the measurement at the thicker part of the specimen (19.1 nm) within the QEP model and without low-loss inelastic scattering.

Atomic scattering factors, ionicity. First we check the angular dependence of scattering on the electron atomic scattering factors by using alternative scattering factors for neutral atoms due to Rez *et al.* [27] compared to those of Weickenmeier and Kohl [28], which were used for the simulations shown in Figs. 3 and 4. Electron atomic scattering factors were fitted to the x-ray atomic form factors tabulated by Rez *et al.* after transformation by the Mott-Bethe formula, using the parametrization approach in Ref. [29]. An additional constraint was applied to the amplitudes of the three Lorentzian terms used in order to reproduce the asymptotic behavior of scattering amplitudes for a screened Coulomb potential into large angles, similar to the approach of Weickenmeier and Kohl [28]. We see in Fig. 6(a) that this does not change the relative difference between simulation and experiment significantly. Rez *et al.* also provide scattering factors for ions and we have also made a simulation for fully ionized $SrTiO_3$ with ions Sr^{2+}, Ti^{4+}, and O^{2-}. The simulation with ionic potentials has slightly larger scattering in the dark field than the simulation with neutral atoms, which leads to a lower relative difference of the solid red curve in the plot of Fig. 6(a). However, the deviations are small enough to be treated as insignificant. The relative differences would be even smaller for partial charge transfer, simulated by taking linear combinations of neutral and ionic scattering factors (not shown).

Thermal vibrations. The simulations in Figs. 3 and 4 were carried out using isotropic temperature factors $B = 8\pi^2\langle u^2\rangle$, where $\langle u^2\rangle$ is the mean-square thermal displacement of the atoms, taken from Ref. [30], namely $B(\mathrm{Sr}) = 0.62$ Å^2, $B(\mathrm{Ti}) = 0.44$ Å^2, and $B(\mathrm{O}) = 0.71$ Å^2. In Fig. 6(b) we see the result of varying the temperature factors B over a wide range. These variations destroy the agreement between theory and experiment in the range of scattering angles between 50 and 64 mrad.

Amorphous layers. Amorphous layers of different thickness were assumed to be symmetrically distributed on the top and bottom surfaces of a 19.1-nm-thick $SrTiO_3$ crystal. Amorphous $SrTiO_3$ was modeled approximately by starting from the crystalline model in Ref. [30] and redistributing the atoms in a box $8 \times 8 \times 16$ unit cells in size. In a final step the density of the randomized structure was reduced to

about 70% of the crystalline structure by ensuring distances between atoms of at least 1.6 Å. In Fig. 6(c) we show the effect of adding amorphous layers up to 3.1 nm thick on each surface. While this largely maintains the features in a PACBED pattern, if it raises the simulated values between 35 and 50 mrad sufficiently to match the experiment then it has the effect of spoiling the match between theory and experiment in the range 50–64 mrad.

Static displacements. If we consider random static displacements of the atoms in the specimen (due, for example, to point defects), with root-mean-square displacements varying between 10 and 50 pm, we obtain the results shown in Fig. 6(d). While this disorder has the effect of increased scattering in the low-angle, dark-field region, good agreement cannot be found for all scattering angles in the measured range using a simple model of random static displacements.

We conclude that our model of low-loss inelastic scattering leads to a much better description of the experimental intensity as a function of scattering angle over the full range up to 64 mrad than that effected by ionic bonding, variations in the temperature (Debye-Waller) factors, amorphous layers, or random static displacements. Furthermore, we know *a priori* that low-loss inelastic scattering is fundamental physics which must be included in our modeling of the electron scattering. The total flux issue (lower in experiment, 95.8%, compared to simulation, 97.3%) cannot be resolved by amorphous layers nor static displacements, since their effects lead to a very different dependency of the intensity on scattering angle.

V. SUMMARY AND CONCLUSIONS

The major advance enabled by the inclusion of low-loss inelastic scattering in the simulation is an almost perfect agreement with the experiment for intensities over all scattering angles beyond the incident probe convergence angle. The insets of Figs. 3(b) and 4(b) show that a relative systematic error in simulations of approximately 25% and 15% has been resolved over a part of the angular range respectively. Residual differences remain below 10% and 5% relative to the measurement. Further improved modeling of inelastic scattering could be achieved by using multiple sets of mean free paths, characteristic angles, and critical angles corresponding to different transitions. However, the approach to simulate the global effect of inelastic scattering with a single parameter set proved to be satisfactory in the present case, although consideration could be given to making the mean free path depth (slice) dependent.

There are similarities between the experimental results for the 9.8- and 19.1-nm-thick $SrTiO_3$ samples presented here and those previously reported for much thicker (around 50 to 150 nm) semiconductor crystals [11]. In particular, for the experimental results shown in Fig. 1, simulations in the QEP (or alternatively a frozen phonon) model and experiments agree for large scattering angles, whereas QEP simulations underestimate scattering for a range of angles starting outside the probe convergence angle. The discrepancy between experiment and theory can be resolved by including low-loss inelastic scattering in the simulations, leading to a redistribution of electrons from the bright field to the lower-angle dark field. Our experiments with $SrTiO_3$ confirm the lower intensity in the bright field observed by Mkhoyan *et al.* [10] and predicted by theory.

The inclusion of low-loss inelastic scattering has led to a remarkable improvement in modeling the angular distribution of scattered electron intensity. In particular, in the low-angle dark-field region almost perfect agreement between experiment and simulation is obtained on an absolute intensity scale. This will be even more important for determining the physical properties of materials specimens thicker than the relatively thin $SrTiO_3$ specimens used here. Although the effect of inelastic scattering can be largely avoided in principle by recording "zero-loss filtered" diffraction patterns, fast pixelated detectors for recording post an image filter are currently not widely available. Also, the usual postmagnification of image filters may restrict access to larger scattering angles.

Although having some effect on the scattering as a function of angle, ionic bonding, changing thermal vibration parameters, adding amorphous surface layers or including static atomic displacements (disorder), did not satisfactorily account for differences between simulation and experiment. A remaining significant mismatch of the total flux of electrons in the recorded angular range, which could not be modeled by simulations including low-loss inelastic scattering or any of the other effects listed above, is on the order of a few percent and warrants further investigation.

Direct consequences of neglecting low-loss inelastic scattering could be expected for the accuracy of thickness determination based on PACBED pattern matching [24,31], especially for thicker samples and, in particular, on the training of neural networks to automate such determinations [32,33]. Since intensity redistribution due to low-loss inelastic scattering is mainly from the bright field towards the low angle dark field, the quantitative analysis of images acquired from these angular regimes are expected to greatly benefit from including the effect in simulations. Another example of a technique where this has ramifications is the measurement of nanometer-scale electric fields in STEM using segmented detectors [34]. Further nontrivial implications for quantitative STEM imaging, which is often limited to thin samples, can be inferred for applications using thicker samples due to the increasing importance of probe channeling and inelastic scattering. As discussed in Ref. [12], the channeling in crystals at or near a zone-axis orientation can be substantially affected if a significant portion of the beam is inelastically scattered. At atomic scale, elemental mapping by means of electron energy-loss and x-ray spectroscopy from inner-shell ionization is known to be sensitive to the channeling of the probe [35]. Therefore, the inclusion of low-loss inelastic scattering is important for quantitative modeling of such elemental maps to measure local elemental concentrations, where thicker specimens are often used to improve the signal-to-noise ratio. While such effects may be suppressed to some extent in PACBED experiments, due to the averaging over probe positions, they will be important when analyzing angle resolved STEM data as a function of probe position at atomic resolution.

ACKNOWLEDGMENTS

We thank K. Müller-Caspary (Forschungszentrum Jülich) for drawing this problem to our attention. We also thank

M. Waschk (Forschungszentrum Jülich) for kindly providing the sample material and H. Quiney (University of Melbourne) for helpful discussions. M.C. acknowledges funding from the Jülich-University of Melbourne Postgraduate Academy (JUMPA). B.G.M. acknowledges funding from the North East Centre for Energy Materials, NECEM (Grant No. EP/R021503/1). S.D.F. was supported by the Australian Research Council (Grant No. DP160102338). L.J.A. acknowledges support by the Alexander von Humboldt-Stiftung.

[1] S. J. Pennycook and P. D. Nellist, *Scanning Transmission Electron Microscopy: Imaging and Analysis* (Springer Science & Business Media, New York, 2011).

[2] S. J. Pennycook and L. A. Boatner, Chemically sensitive structure-imaging with a scanning transmission electron microscope, Nature (London) **336**, 565 (1988).

[3] J. M. LeBeau, S. D. Findlay, L. J. Allen, and S. Stemmer, Quantitative Atomic Resolution Scanning Transmission Electron Microscopy, Phys. Rev. Lett. **100**, 206101 (2008).

[4] B. D. Forbes, A. V. Martin, S. D. Findlay, A. J. D'Alfonso, and L. J. Allen, Quantum mechanical model for phonon excitation in electron diffraction and imaging using a Born-Oppenheimer approximation, Phys. Rev. B **82**, 104103 (2010).

[5] G. McMullan, A. R. Faruqi, D. Clare, and R. Henderson, Comparison of optimal performance at 300 keV of three direct electron detectors for use in low dose electron microscopy, Ultramicroscopy **147**, 156 (2014).

[6] C. Ophus, Four-dimensional scanning transmission electron microscopy (4D-STEM): From scanning nanodiffraction to ptychography and beyond, Microsc. Microanal. **25**, 563 (2019).

[7] Z. Yu, D. A. Muller, and J. Silcox, Study of strain fields at a-Si / c-Si interface, J. Appl. Phys. **95**, 3362 (2004).

[8] L. Fitting, S. Thiel, A. Schmehl, J. Mannhart, and D. A. Muller, Subtleties in ADF imaging and spatially resolved EELS: A case study of low-angle twist boundaries in $SrTiO_3$, Ultramicroscopy **106**, 1053 (2006).

[9] S. D. Findlay, N. Shibata, H. Sawada, E. Okunishi, Y. Kondo, and Y. Ikuhara, Dynamics of annular bright field imaging in scanning transmission electron microscopy, Ultramicroscopy **110**, 903 (2010).

[10] K. A. Mkhoyan, S. E. Maccagnano-Zacher, M. G. Thomas, and J. Silcox, Critical Role of Inelastic Interactions in Quantitative Electron Microscopy, Phys. Rev. Lett. **100**, 025503 (2008).

[11] K. Müller-Caspary, O. Oppermann, T. Grieb, F. F. Krause, A. Rosenauer, M. Schowalter, T. Mehrtens, A. Beyer, K. Volz, and P. Potapov, Materials characterisation by angle-resolved scanning transmission electron microscopy, Sci. Rep. **6**, 37146 (2016).

[12] B. G. Mendis, An inelastic multislice simulation method incorporating plasmon energy losses, Ultramicroscopy **206**, 112816 (2019).

[13] R. A. Ferrell, Characteristic energy loss of electrons passing through metal foils. II. Dispersion relation and short wavelength cutoff for plasma oscillations, Phys. Rev. **107**, 450 (1957).

[14] R. F. Egerton, *Electron Energy-loss Spectroscopy in the Electron Microscope* (Springer Science & Business Media, New York, 2011).

[15] J. C. H. Spence, in *High-Resolution Transmission Electron Microscopy: and Associated Techniques*, edited by P. Buseck, J. Cowley, and L. Eyring (Oxford University Press, New York, 1989).

[16] J. Stiebling and H. Raether, Dispersion of the Volume Plasmon of Silicon (16.7 eV) at Large Wave Vectors, Phys. Rev. Lett. **40**, 1293 (1978).

[17] J. Barthel, Dr. Probe: A software for high-resolution STEM image simulation, Ultramicroscopy **193**, 1 (2018).

[18] L. J. Allen, A. J. D'Alfonso, and S. D. Findlay, Modelling the inelastic scattering of fast electrons, Ultramicroscopy **151**, 11 (2015).

[19] T. W. Josefsson, R. L. Cobal, and L. J. Allen, Dielectric matrix calculation of the differential cross section for plasmon excitation and application to electron diffraction, Phys. Rev. B **54**, 12873 (1996).

[20] H. Watanabe, Experimental evidence for the collective nature of the characteristic energy loss of electrons in solids – studies on the dispersion relation of plasma frequency, J. Phys. Soc. Jpn. **11**, 112 (1956).

[21] M. Heggen, M. Luysberg, and K. Tillmann, Ernst Ruska-Centre for microscopy and spectroscopy with electrons (ER-C), FEI Titan 80-300 STEM, J. Large-scale Res. Facil. **2**, A42 (2016).

[22] G. W. Paterson, R. J. Lamb, R. Ballabriga, D. Maneuski, V. O'Shea, and D. McGrouther, Sub-100 nanosecond temporally resolved imaging with the Medipix3 direct electron detector, Ultramicroscopy **210**, 112917 (2020).

[23] M. Kruth, D. Meertens, and K. Tillmann, Ernst Ruska-Centre for microscopy and spectroscopy with electrons (ER-C), FEI Helios NanoLab 460F1 FIB-SEM, J. Large-scale Res. Facil. **2**, A59 (2016).

[24] J. A. Pollock, M. Weyland, D. J. Taplin, L. J. Allen, and S. D. Findlay, Accuracy and precision of thickness determination from position-averaged convergent beam electron diffraction patterns using a single-parameter metric, Ultramicroscopy **181**, 86 (2017).

[25] K. van Benthem, R. H. French, W. Sigle, C. Elsässer, and M. Rühle, Valence electron energy loss study of Fe-doped $SrTiO_3$ and a $\Sigma 13$ boundary: Electronic structure and dispersion forces, Ultramicroscopy **86**, 303 (2001).

[26] K. van Benthem, C. Elsässer, and R. H. French, Bulk electronic structure of $SrTiO_3$: Experiment and theory, J. Appl. Phys. **90**, 6156 (2001).

[27] D. Rez, P. Rez, and I. Grant, Dirac–Fock calculations of X-ray scattering factors and contributions to the mean inner potential for electron scattering, Acta Crystallogr., Sect. A **50**, 481 (1994).

[28] A. Weickenmeier and H. Kohl, Computation of absorptive form factors for high-energy electron diffraction, Acta Crystallogr., Sect. A **47**, 590 (1991).

[29] E. J. Kirkland, *Advanced Computing in Electron Microscopy* (Springer Science & Business Media, New York, 2010).

[30] Y. A. Abramov, V. G. Tsirelson, V. E. Zavodnik, S. A. Ivanov, and I. D. Brown, The chemical bond and atomic displacements

in $SrTiO_3$ from X-ray diffraction analysis, Acta Crystallogr., Sect. B **51**, 942 (1995).

[31] J. M. LeBeau, S. D. Findlay, L. J. Allen, and S. Stemmer, Position averaged convergent beam electron diffraction: Theory and applications, Ultramicroscopy **110**, 118 (2010).

[32] W. Xu and J. M. LeBeau, A deep convolutional neural network to analyze position averaged convergent beam electron diffraction patterns, Ultramicroscopy **188**, 59 (2018).

[33] C. Zhang, J. Feng, L. R. DaCosta, and P. M. Voyles, Atomic resolution convergent beam electron diffraction analysis using convolutional neural networks, Ultramicroscopy **210**, 112921 (2019).

[34] H. G. Brown, N. Shibata, H. Sasaki, T. C. Petersen, D. M. Paganin, M. J. Morgan, and S. D. Findlay, Measuring nanometre-scale electric fields in scanning transmission electron microscopy using segmented detectors, Ultramicroscopy **182**, 169 (2017).

[35] Y. Zhu, A. Soukiassian, D. G. Schlom, D. A. Muller, and C. Dwyer, Towards artifact-free atomic-resolution elemental mapping with electron energy-loss spectroscopy, Appl. Phys. Lett. **103**, 141908 (2013).